



The dynamics of MEMS-Colpitts oscillators

Shreyas Y. Shah · Nikhil Bajaj · Conor Pyles ·
Dana Weinstein · Jeffrey F. Rhoads ·
D. Dane Quinn

Received: 20 July 2022 / Accepted: 9 July 2023 / Published online: 18 August 2023
© The Author(s), under exclusive licence to Springer Nature B.V. 2023

Abstract Microelectromechanical systems (MEMS) based oscillators have been proposed for use in coupled arrays for many applications, including neuromorphic computing, clocks with reduced phase noise, and sensors. In many prior studies, the models for coupled oscillator behavior depended upon the phase dynamics of the individual oscillators, while the amplitude dynamics were assumed to be negligible. However, implementation of practical large-scale MEMS oscillator networks may involve systems with significant amplitude dynamics. This cannot be described by the commonly used phase models or by steady-state models that do not predict transient behavior. We present the design and analysis of a MEMS-Colpitts oscillator topology suitable for monolithic integration (resonators with integrated circuits). Applying multiple

scales analysis to the dynamics results in significantly faster computation as compared to direct integration and enables the study of nonlinear behaviors (e.g. bifurcations) and both amplitude and phase dynamics. The strong correlation between the analytical and experimental results demonstrates the effectiveness of our modelling approach.

Keywords Micromechanical systems · Oscillators · Nonlinear dynamical systems · Multiple scales

1 Introduction

Coupled oscillator arrays have attracted attention for a number of applications, such as clocks with reduced phase noise [1], digital clock distribution [2], sensor systems [3], and neuromorphic computing [4–8]. Oscillators in such arrays are often represented using Kuramoto-style models, such as those presented by Hoppensteadt and Izhekevich, [5,6,9,10] which account solely for phase dynamics. Even though these models serve to explain major aspects of system dynamics [11], nonlinearities inherent to real oscillators [12–14] make it difficult to ignore the role played by amplitude dynamics in these systems [1,15–18]. Therefore, in order to design and analyse physical oscillator networks, it is necessary to first develop oscillator models, based on real-world implementations, incorporating the nonlinearities and associated amplitude dynamics, without significantly adding to the com-

S. Y. Shah · D. Weinstein
School of Electrical and Computer Engineering, Purdue University, West Lafayette, IN 47907, USA
e-mail: danaw@purdue.edu

N. Bajaj (✉)
Department of Mechanical Engineering and Materials Science, University of Pittsburgh, Pittsburgh, PA 15261, USA
e-mail: nbajaj@pitt.edu

C. Pyles · J. F. Rhoads
School of Mechanical Engineering, Purdue University, West Lafayette, IN 47907, USA
e-mail: jfrhoads@purdue.edu

D. D. Quinn
Department of Mechanical Engineering, University of Akron, Akron, OH 44325, USA
e-mail: quinn@uakron.edu

putational load. In addition, before an array of coupled oscillators can be modeled, the single oscillator's behavior must be carefully modeled in a computationally efficient way. This is the focus of this work.

Microelectromechanical (MEMS) oscillators are a potential platform to implement scalable oscillator networks [19–23]. These devices can be designed to have excellent performance due to the high-quality factors (Q) of their electromechanical resonant elements. Compact, monolithically integrated MEMS-Colpitts and Pierce oscillators (differing in their feedback topology and nonlinear elements) have recently been demonstrated on gallium nitride (GaN) [19]. However, the time and expense associated with the fabrication of these monolithically integrated circuits (MMICs), combined with the difficulty in designing and simulating complex nonlinear oscillator networks, makes it challenging to reliably implement oscillator networks at the scale required for applications such as neuromorphic computing. Because the design and manufacturing is currently quite involved, improved tools for studying the complex behavior of these networks (and their component oscillator elements) would be useful in the process of oscillator system design.

In this work, we study the dynamics of a Colpitts oscillator designed using a MEMS resonator and a high-electron-mobility transistor (HEMT). The relative simplicity of the Colpitts topology over the Pierce topology (in the context of the GaN-MMIC platform [19]), attributable to the lower component count, and a zero voltage bias on the piezoelectric MEMS resonator, simplifies the implementation. While this class of oscillator can display rich, complex, and potentially problematic dynamical behavior (e.g. chaos) [24, 25], previous work has generated guidelines as to how to avoid these operating regions [26]. This work presents the design of a Colpitts oscillator similar to [19] (see Fig. 1) that was implemented as an MMIC, and investigates the dynamical behavior of an appropriate model using multiple scales analysis. The approach presented in this work also enables the study of transient dynamics. Some analytical studies have been performed on MEMS-based oscillator systems in the past (for example, the work by Agrawal, Woodhouse, and Seshia [27, 28]), which incorporate amplitude dynamics using an averaging method. Our study is distinguishable from such works due to the circuits and resonators being quite different, as well as the method of nonlinear anal-

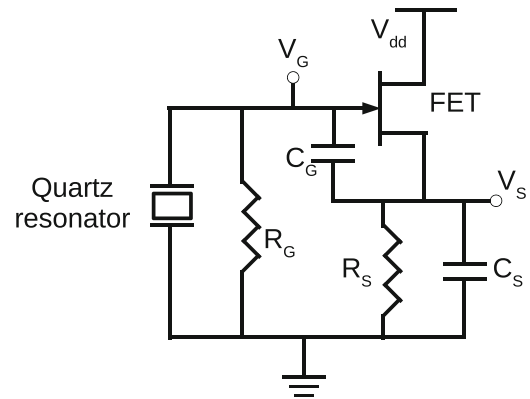


Fig. 1 Schematic diagram of the MEMS-Colpitts oscillator. The quartz resonator is connected to the gate of the FET (HEMT). Unity gain buffers, not shown, are used to measure signals at the V_G and V_S nodes without significantly electrically loading the oscillator circuit. The input resistance and capacitance of the buffers are included in the parameters given in Eq. 14

ysis being distinct. In addition, the approach presented here can address arbitrary nonlinearities in the transistor model, which represents the nonlinear element of the oscillator system.

The results of the analysis are compared with direct numerical simulation of the underlying model, as well as experimental measurements obtained from an oscillator board. The chief contribution in this paper is the aforementioned incorporation of transient amplitude dynamics in the modelling and the subsequently generated understanding of the dynamics of a single MEMS-Colpitts oscillator. This is particularly important towards the end goal of efficiently modelling the behavior of networked arrays of coupled MEMS-Colpitts oscillators that can be employed in neuromorphic computing, synchronized clock systems, and other applications.

In what follows below, the Methods section (Sect. 2) of the paper describes the design of the oscillator and the derivation of the corresponding equations of motion. The application of the method of multiple scales to this system is also presented. In Sect. 3 (Resonator Dynamics), the results of the multiple scales modelling approach are discussed and compared to the dynamics obtained through direct numerical integration of the original equations of motion. Section 4, Experimental Comparison, confirms the operation of the physical oscillator system and the ability of the multiple scales analysis to capture important qualitative aspects of the behavior of the physical system,

including both the steady-state amplitude of the time-dependent oscillations as well as the transient growth rate. In particular, the dynamic behavior of the system is considered as the drain current gain is varied, including the stability of the equilibrium solution and the amplitude of the steady-state oscillations. Finally, the discussion and conclusions discuss potential limitations and further developments of the analytical approach, as well as the oscillator technology.

2 Methods

2.1 Design of the MEMS-Colpitts oscillator

In order to study the dynamics of the MEMS-Colpitts topology, an oscillator was designed (see Fig. 1) based on a 16 MHz quartz crystal resonator (Kyocera CX322-5CA) and a gallium arsenide (GaAs) HEMT (Avago ATF-35143). The equivalent three-point oscillator circuit was used to design the feedback loop of a Colpitts oscillator to have sufficient negative resistance [29] to satisfy the Barkhausen criterion, compensate for resonator losses, and sustain oscillations. As mentioned, the Colpitts topology was chosen due to its low component count and relative simplicity. As a practical matter, unity gain buffers were used to ensure consistency of measurement and operation and were applied at the gate and source nodes, whose potentials are the field-effect transistor (FET) gate voltage V_G and FET source voltage V_S , respectively. The buffer amplifiers were implemented using Texas Instruments LMH6609 operational amplifiers, and the input impedance of these is considered in the parameter estimates for R_G , C_G , R_S , and C_S . The required resistance and capacitance values were estimated using three-point oscillator theory and confirmed in simulation (Cadence Spectre) before the hardware implementation.

The Butterworth-van Dyke (BVD) model was used to represent the quartz crystal resonator and is shown in Fig. 2 with the corresponding measured power transmission spectrum. The crystals have a typical quality factor (Q) between 40,000 and 80,000 depending on the specific device. This representation accurately models the linear resonator dynamics near resonance. In the derivation that follows, only the motional branch (consisting of motional resistance R_M , motional capacitance C_M , and motional inductance L_M , connected

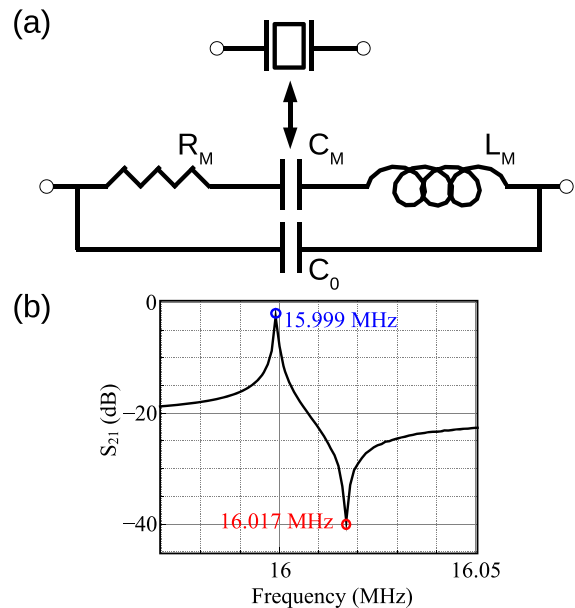


Fig. 2 **a** The Butterworth-van Dyke model used for the resonator in the circuit simulations. **b** The model parameters were estimated from the power-transmission spectrum of the resonator

to the electromechanical response of the piezoelectric resonator), was considered in the model, as the shunt capacitance C_0 was negligible as compared to C_G and C_S . Such resonators can display hardening non-linearity at high drive amplitudes; however, the effect is relatively small and we ignore this in the analysis. Note that microfabricated MEMS oscillators can operate at frequencies into the GHz range, and the corresponding dynamical equations for the high-frequency and ultrahigh-frequency oscillators are different even when the circuit architecture is consistent. Resonators with useful resonant modes in the GHz range are commonly characterized using a modified Butterworth-van Dyke (mBvD) model [30–32], which consists of a two-branch lumped parameter circuit. However, the solution methodology presented here can be extended to mBvD and other lumped parameter model variants by incorporating additional states. In the present work, the simpler model BvD model is chosen, which is appropriate for the resonator described above.

2.2 Equations of motion: derivation and nondimensionalization

Given the design noted above, differential equations are derived to describe operation by first applying Kirchhoff's current law at the V_G and V_S nodes:

$$C_G \dot{V}_G - C_G \dot{V}_S = -\frac{V_G}{R_G} - I_M \quad (1)$$

$$C_G \dot{V}_G - (C_G + C_S) \dot{V}_S = \frac{1}{R_S} V_S - I_D. \quad (2)$$

Here, I_D is the current through the FET and I_M is the motional equivalent current through the resonator, both measured in Amperes. We define a dynamical variable F , such that $I_M \equiv C_M F$. Kirchhoff's current law is then applied to the internal nodes of the motional branch of the resonator, so that

$$L_M C_M \ddot{F} = -F + \dot{V}_G - R_M C_M \dot{F}. \quad (3)$$

The behavior of the FET in the design can be well described using the Statz MESFET model when the value of $V_G - V_S$ is above the threshold voltage V_{th} [33] (see Figs. 3 and 4). The $(V_G - V_S)$ quantity does not exceed -0.6 V in operation. For sufficiently large values of $(V_{dd} - V_S)$, which is true for the voltage range in which this circuit operates,

$$I_D = \beta \frac{((V_G - V_S) - V_{th})^2}{B((V_G - V_S) - V_{th}) + 1} [1 + \lambda(V_{dd} - V_S)]. \quad (4)$$

Here, $V_{th} = -0.95$ V, $\beta = 0.12$ A V⁻², $B = 0.8$ V⁻¹, and $\lambda = 0.09$ V⁻¹ are semi-empirical model parameters specified in the ATF-35143 device datasheet [34]. When $V_G - V_S < V_{th}$, the drain current can be modeled as identically zero (the off state).

In the region where $V_G - V_S \geq V_{th}$, this expression can be expanded in series form as,

$$I_D = \beta((V_G - V_S) - V_{th})^2 [1 - b((V_G - V_S) - V_{th})][1 + \lambda(V_{dd} - V_S)] + \mathcal{O}[(V_G - V_S - V_{th})^4]. \quad (5)$$

Restricting the analysis to the lowest order of nonlinearity in the FET, the experimental drain current can be written as a piecewise continuous function, in the form

$$I_D = \begin{cases} \beta((V_G - V_S) - V_{th})^2, & (V_G - V_S) - V_{th} > 0 \\ 0, & (V_G - V_S) - V_{th} \leq 0 \end{cases}. \quad (6)$$

This results in the common quadratic form of the equation for currents passing through the FETs and lends

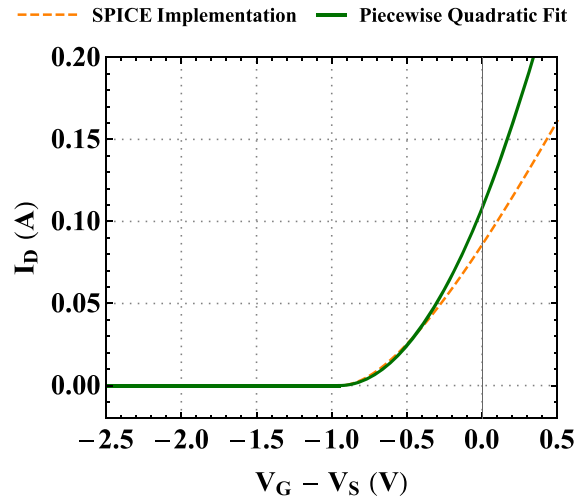


Fig. 3 The drain current model [Eq. (4)] compares well with the behavior of the FET as simulated using Cadence Spectre using the parameters specified in the datasheet. The deviation at higher (and lower) voltages is due to the gate-leakage current (and sub-threshold behavior), which is not included in this work's model

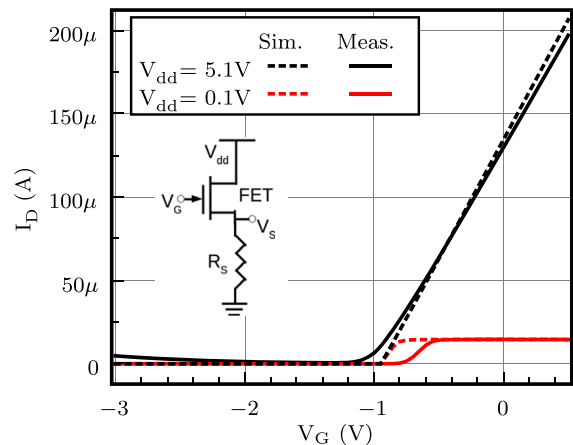


Fig. 4 The measured drain current of an ATF-35143 FET matches the current from circuit simulations in Cadence Spectre, over a wide range of supply voltages, confirming the reliability of our SPICE model

our analysis to other potential implementations on different platforms.

Summarizing the above, the dynamics of a single MEMS-Colpitts oscillator can be described as

$$L_M \ddot{F} + R_M \dot{F} + \frac{1}{C_M} F = \frac{1}{C_M} \dot{V}_G, \quad (7a)$$

$$C_G \dot{V}_G - C_G \dot{V}_S = -\frac{1}{R_G} V_G - C_M F, \quad (7b)$$

$$C_G \dot{V}_G - (C_G + C_S) \dot{V}_S = \frac{1}{R_S} V_S - I_D((V_G - V_S) - V_{th}). \quad (7c)$$

Note that the relationship between the gain current I_D and the supply voltages remains general. These equations can be nondimensionalized by scaling time, together with the variables (F, V_G, V_S) as

$$t = \left(\sqrt{L_M C_M} \right) \tau, \quad F = \left(\frac{|V_{th}| \sqrt{C_G/C_M}}{\sqrt{L_M C_M}} \right) f, \\ V_G = (|V_{th}|) v, \quad V_S = (|V_{th}|) u, \quad (8)$$

so that the nondimensional equations of motion become

$$f'' + \varepsilon^2 \lambda f' + f = \varepsilon v', \quad (9a)$$

$$(v' - u') + \alpha_1 v = -\varepsilon f, \quad (9b)$$

$$-\mu (v' - u') + u' + \alpha_2 u = g(v - u \pm 1), \quad (9c)$$

where g is the nondimensional drain current. In the argument of g , the ± 1 is chosen based on the sign of V_{th} . With $V_{th} < 0$ the argument is $v - u + 1$, and in what follows this form is retained. Note that in these equations of motion the damping coefficient for f has been scaled by ε^2 . The resulting nondimensional parameters are defined as

$$\mu = \frac{C_G}{C_S}, \quad \alpha_1 = \frac{\sqrt{L_M C_M}}{C_G R_G}, \quad \alpha_2 = \frac{\sqrt{L_M C_M}}{C_S R_S}, \\ \varepsilon = \sqrt{\frac{C_M}{C_G}}, \quad \lambda = \frac{R_M C_G}{\sqrt{L_M C_M}}, \quad (10)$$

while the nondimensional drain current g is related to the I_D as

$$g(v - u + 1) \equiv \frac{\sqrt{L_M C_M}}{|V_{th}| C_S} I_D \left(|V_{th}| (v - u + 1) \right). \quad (11)$$

so that the resulting nondimensional function becomes

$$g = \begin{cases} \gamma (v - u + 1)^2, & v - u + 1 \geq 0 \\ 0, & v - u + 1 < 0 \end{cases}, \quad (12)$$

where the nondimensional gain is defined as

$$\gamma = \frac{\beta |V_{th}| \sqrt{L_M C_M}}{C_S}. \quad (13)$$

The system is simulated with dimensional parameters corresponding to the nominal experimental system described below in Sect. 4, identified as

$$C_M = 2.201 \times 10^{-15} \text{ F}, \quad R_M = 5.62 \times 10^1 \Omega, \\ C_S = 1.62 \times 10^{-11} \text{ F}, \quad R_S = 7.444 \times 10^3 \Omega, \\ C_G = 2.32 \times 10^{-11} \text{ F}, \quad R_G = 5.168 \times 10^4 \Omega, \\ L_M = 4.496 \times 10^{-2} \text{ H}, \quad V_{th} = -9.50 \times 10^{-1} \text{ V}, \quad (14)$$

so that the corresponding nominal nondimensional parameters are

$$\mu = 1.432, \quad \alpha_1 = 8.249 \times 10^{-3}, \quad \alpha_2 = 8.249 \times 10^{-2}, \\ \varepsilon = 9.74 \times 10^{-3}, \quad \lambda = 1.311 \times 10^{-1}, \quad \gamma = 7.0024 \times 10^1. \quad (15)$$

In particular, we note that the numerical value of λ corresponding to the experimental parameters is $\mathcal{O}(1)$, so that the $\mathcal{O}(\varepsilon^2)$ scaling applied to the resonator dissipation term is appropriate. In addition, the parameter values for those components interacting with the V_G and V_S nodes have been slightly modified to incorporate the effect of the unity gain buffer amplifiers on the circuit, by computing the equivalent values that incorporate the input impedance of the buffer amplifiers (nominal parallel input resistance of $1.2 \text{ M}\Omega$ and capacitance of 1.2 pF). Finally, although the numerical values of the time constants α_1 and α_2 that correspond to the experimental system are small, these terms are nonetheless retained for generality in the ensuing analysis.

2.3 Multiple scales analysis

We introduce multiple timescales into the above nondimensional equations of motion to second order, so that

$$\eta_0 = \tau, \quad \eta_1 = \varepsilon \tau, \quad \eta_2 = \varepsilon^2 \tau, \quad \longrightarrow \quad \frac{d}{d\tau} \\ = \frac{\partial}{\partial \eta_0} + \varepsilon \frac{\partial}{\partial \eta_1} + \varepsilon^2 \frac{\partial}{\partial \eta_2}, \quad (16)$$

while

$$f(\eta_0) = f_0(\eta_0) + \varepsilon f_1(\eta_0) + \varepsilon^2 f_2(\eta_0) + \dots, \\ v(\eta_0) = v_0(\eta_0) + \varepsilon v_1(\eta_0) + \varepsilon^2 v_2(\eta_0) + \dots, \quad (17) \\ u(\eta_0) = u_0(\eta_0) + \varepsilon u_1(\eta_0) + \varepsilon^2 u_2(\eta_0) + \dots.$$

In this notation, the set of independent times scales is represented as $\boldsymbol{\eta}_i \equiv (\eta_i, \eta_{i+1}, \dots)$ (note the bold font). Therefore, for example, $\boldsymbol{\eta}_1$ represents a dependence on all of the timescales at or slower than η_1 . In addition,

the nonlinear drain current can be expressed as $g = g_0 + \varepsilon g_1$, with

$$g_0 \equiv g(v_0 - u_0 + 1) \\ \varepsilon g_1 \equiv g((v_0 - u_0 + 1) + \varepsilon(v_1 - u_1)) \quad (18a)$$

$$- g(v_0 - u_0 + 1). \quad (18b)$$

Note that to lowest order g_1 represents the $\mathcal{O}(\varepsilon)$ expansion of the nonlinear function. However, as written g_1 also contains additional higher-order terms that will be important for the long-term dynamics of the system.

Collecting terms of Eq. (9) to lowest order in ε yields

$$\frac{\partial^2 f_0}{\partial \eta_0^2} + f_0 = 0, \quad (19a)$$

$$\frac{\partial v_0}{\partial \eta_0} - \frac{\partial u_0}{\partial \eta_0} + \alpha_1 v_0 = 0, \quad (19b)$$

$$- \frac{\partial v_0}{\partial \eta_0} + (1 + \mu) \frac{\partial u_0}{\partial \eta_0} + \alpha_2 u_0 = g_0. \quad (19c)$$

As $\eta_0 \rightarrow \infty$ the functions (u_0, v_0) decay exponentially, approaching a steady-state solution. For the piecewise continuous function given in Eq. (12), the equilibrium equations reduce to

$$\alpha_1 v_0 = 0, \quad \alpha_2 u_0 = \gamma (v_0 - u_0 + 1)^2, \quad (20)$$

provided $v_0 - u_0 + 1 \geq 0$. The resulting equilibrium state is given by $v_0 = 0$, and

$$u_0 = \left(1 + \frac{\alpha_2}{2\gamma}\right) - \sqrt{\left(1 + \frac{\alpha_2}{2\gamma}\right)^2 - 1}. \quad (21)$$

Note that for $\gamma > 0$ the second solution to the quadratic equilibrium equation violates the above inequality so that $g_0 \equiv 0$. The solution for $f_0(\eta_0)$ can be written as

$$f_0(\eta_0) = A_0(\eta_1) \sin[\eta_0 + \phi_0(\eta_1)], \quad (22)$$

so that the functions (A_0, ϕ_0) vary on the slow timescales η_1 and represent the slowly varying amplitude and phase of the $\mathcal{O}(1)$ solution.

At $\mathcal{O}(\varepsilon)$, the perturbative equations for f , given in Eq. (9a), reduce to

$$\frac{\partial^2 f_1}{\partial \eta_0^2} + f_1 = -2 \frac{\partial^2 f_0}{\partial \eta_0 \partial \eta_1}, \quad (23) \\ = -2 \left[\frac{\partial A_0}{\partial \eta_1} \cos \psi_0 - A_0 \frac{\partial \phi_0}{\partial \eta_1} \sin \psi_0 \right],$$

where $\psi_0(\eta_0) \equiv \eta_0 + \phi_0(\eta_1)$ is notation for the argument of the harmonic term in the $\mathcal{O}(1)$ solution for f_0 , given in Eq. (22). Removal of secular terms requires that

$$\frac{\partial A_0}{\partial \eta_1} = 0, \quad \frac{\partial \phi_0}{\partial \eta_1} = 0. \quad (24)$$

Therefore both A_0 and ϕ_0 are constant on the η_1 timescale, so that

$$A_0 = A_0(\eta_2), \quad \phi_0 = \phi_0(\eta_2). \quad (25)$$

Without loss of generality, we assume that $f_1(\eta_0) \equiv 0$.

Turning to $\mathcal{O}(\varepsilon^2)$, expanding Eq. (9a) yields

$$\frac{\partial^2 f_2}{\partial \eta_0^2} + f_2 = \frac{\partial v_1}{\partial \eta_0} - \lambda \frac{\partial f_0}{\partial \eta_0} - \frac{\partial^2 f_0}{\partial \eta_1^2} - 2 \frac{\partial^2 f_0}{\partial \eta_0 \partial \eta_2}, \\ = \frac{\partial v_1}{\partial \eta_0} - \lambda A_0 \cos \psi_0 \quad (26) \\ - 2 \left[\frac{\partial A_0}{\partial \eta_2} \cos \psi_0 - A_0 \frac{\partial \phi_0}{\partial \eta_2} \sin \psi_0 \right].$$

The solution for $\frac{\partial v_1}{\partial \eta_0}$ is required to identify the secular terms and ultimately determine the evolution of A_0 and ϕ_0 on the slow timescale.

Returning to $\mathcal{O}(\varepsilon)$, the equations for (u_1, v_1) from Eqs. (9b,c) are

$$\frac{\partial v_1}{\partial \eta_0} - \frac{\partial u_1}{\partial \eta_0} + \alpha_1 v_1 = -A_0 \sin \psi_0, \quad (27a)$$

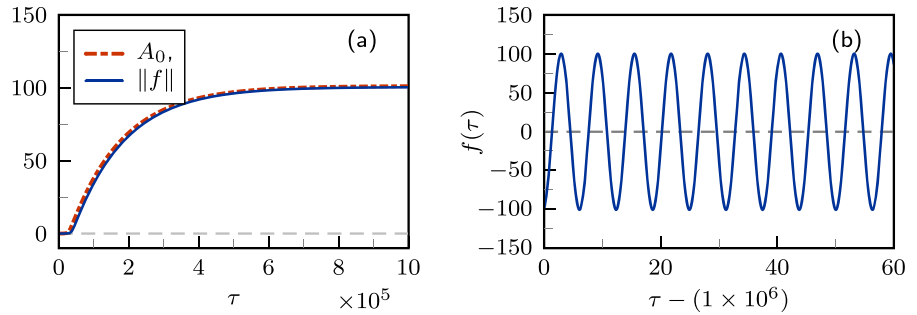
$$- \mu \frac{\partial v_1}{\partial \eta_0} + (1 + \mu) \frac{\partial u_1}{\partial \eta_0} + \alpha_2 u_1 = g_1. \quad (27b)$$

For the nondimensional drain current given in Eq. (12), g_1 reduces to

$$g_1 = \gamma \cdot \begin{cases} (v_1 - u_1) [2(1 - u_0) \\ + \varepsilon(v_1 - u_1)], & \varepsilon(v_1 - u_1) \geq u_0 - 1, \\ -\frac{1}{\varepsilon}(1 - u_0)^2, & \varepsilon(v_1 - u_1) < u_0 - 1. \end{cases} \quad (28)$$

Notice that g_1 contains terms depending on ε that arise from the quadratic terms in the original equations of motion. A standard perturbation approach would push these terms out to the next order in the expansion. However, investigation of the response of the original system of equations indicates that these nonlinearities are responsible for limiting the growth of the response and are therefore included at this order. The resulting approach is no longer formally asymptotic, but the inclusion of these terms will be justified later when the response of the slow-flow equations are compared

Fig. 5 Numerical simulation of the nondimensional equations of motion; **a** amplitude: A_0 —Eq. (30) averaged equations, $\|f\|$ —Eq. (9) nondimensional equations; **b** stationary response of $f(\tau)$: Eq. (9) nondimensional equations



with that of the original equations of motion. This system will provide a qualitatively accurate description of the observed numerical response of Eqs. (9).

This system can be solved on the η_0 timescale using a harmonic balance approach to incorporate the piecewise quadratic nonlinearity [35], where (u_1, v_1) are approximated as

$$\begin{aligned} u_1(\eta_0) &= U(\eta_1) + X(\eta_1) \cos[\eta_0 + \phi_0(\eta_1)] \\ &\quad + Y(\eta_1) \sin[\eta_0 + \phi_0(\eta_1)], \\ v_1(\eta_0) &= V(\eta_1) + G(\eta_1) \cos[\eta_0 + \phi_0(\eta_1)] \\ &\quad + H(\eta_1) \sin[\eta_0 + \phi_0(\eta_1)], \end{aligned} \quad (29)$$

with $\psi_0(\eta_0) \equiv \eta_0 + \phi_0(\eta_1)$. Therefore, in Eq. (27) the coefficients of the constant, cosine, and sine terms are collected and eliminated. The resulting algebraic equations that determine the harmonic balance coefficients are described in Eq. (33) of Appendix A, providing six algebraic equations that can be solved for (U, V, X, G, Y, H) .

Finally, examining Eq. (26) removal of secular terms yields the evolution equations for amplitude of the resonator as

$$\frac{\partial A_0}{\partial \eta_2} + \frac{1}{2} (\lambda A_0 - H) = 0, \quad (30)$$

while the phase $\phi_0(\eta_1)$ of the resonator is determined from

$$A_0 \frac{\partial \phi_0}{\partial \eta_2} + \left(-\frac{G}{2} \right) = 0, \quad (31)$$

with (G, H) determined from the previous harmonic balance solution for (u_1, v_1) as given in Eq. (29). The instantaneous growth rate on the $\mathcal{O}(1)$ timescale is identified as

$$\sigma = \frac{\varepsilon^2}{2} \left(\frac{H}{A_0} - \lambda \right), \quad (32)$$

and equilibrium solutions for the slow flow equations, which occur for $\sigma = 0$, correspond to stationary periodic solutions in the original equations of motion.

3 Resonator dynamics

With the nominal parameters given in Eq. (15), the time response of $f(\tau)$ is shown in Fig. 5. In Fig. 5a, the amplitude of the response is illustrated from both the averaged equations (red) and from numerical simulation of the nondimensional equations of motion (blue). The observed agreement is excellent in terms of both the transient behavior and the steady-state amplitude of the oscillations. The stationary response of the nondimensional equations given in Eq. (9) is shown in Fig. 5b, and the observed amplitude is $\|f\| = 100.35$, to be compared with the equilibrium amplitude predicted by the multiple scales analysis, which is $A_{0,\text{eq}} = 101.22$. If one computes the amplitude of $v(\eta_1)$ (readily available from the harmonic balance result as $\sqrt{(G^2 + H^2)}$) from this result, the steady state amplitude of V_G when converted to volts is 2.30 V. The nondimensional time corresponding to a 63.2% “rise time constant” (the time to reach 63.2% of the steady state value) is approximately 20,000 units, and this corresponds to 0.00199 s. These quantities will be used to compare to the experimental results.

The computational efficiency of the multiple scales analysis is significantly increased when compared to direct numerical simulation of the original equations of motion. As an example, in Fig. 5 the time required to solve the multiple scales solution from Eq. (30) was approximately 2500 times as fast as that required for the direct numerical simulation of Eq. (9), as measured by MATLAB’s `cputime` function (6340 sec for the direct numerical simulation versus 2.47 sec for the averaged equations).¹ Similar increases in efficiency were seen throughout the analysis.

¹ The computational speed up was observed to scale roughly as $1/\varepsilon^2$.

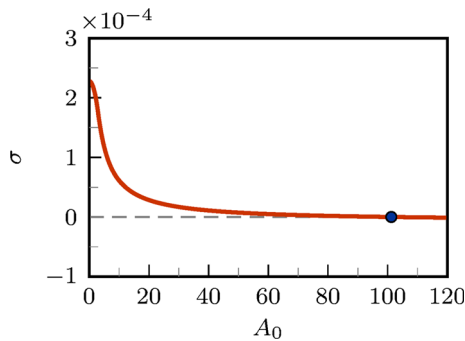


Fig. 6 Instantaneous growth rate σ , as predicted from the multiple scales approach given in Eq. (30). Note that the equilibrium amplitude is predicted to be $A_{0,\text{eq}} = 101.224$, where the growth rate vanishes

Examining Eq. (32), the instantaneous growth rate σ determines the evolution of the amplitude A_0 . Moreover, as shown in Fig. 6, this quantity is a function only of the amplitude A_0 so that Eq. (30) leads to a first-order approximation for the evolution of the amplitude. In particular, the predicted growth rate vanishes for $A_{0,\text{eq}} = 101.22$, which corresponds to a stable steady-state amplitude for the oscillations.

Self-excited oscillations occur when the trivial solution $(f_{\text{eq}}, u_{\text{eq}}, v_{\text{eq}}) \equiv (0, u_0, 0)$ is unstable. Examining the amplitude equation given in Eq. (30), instability of this solution occurs when $\sigma|_{A_0=0} > 0$, and in this limit the exponential growth rate can be evaluated in closed form, as in shown in Eq. (36) of Appendix A. In Fig. 7, the growth rate of the trivial solution is shown as a function of the nondimensional gain γ . Note that for these parameter values, at $\gamma_\star = 0.422$ this growth rate vanishes so that the trivial solution is stable for $\gamma < \gamma_\star$ and unstable for $\gamma > \gamma_\star$. It is for this latter range of parameters that self-excited oscillations are expected to exist in the system.

Finally, the steady-state amplitude for the system can be determined by solving $A_0 \cdot \sigma(A_0) = 0$. Although the trivial solution $A_0 = 0$ exists for all parameter values, non-trivial solutions $\sigma(A_0) = 0$ exist for $\gamma > \gamma_\star$, as illustrated in Fig. 6. In Fig. 8, the bifurcation diagram for the system is shown as the gain γ varies. Stability can be determined from the effective growth rate, σ . As seen in Fig. 6, there exists a bifurcation point at $\gamma = \gamma_\star = 0.422$ where the trivial solution loses stability and a stable solution with nonzero amplitude arises. It should be noted that in many ways this system is qualitatively similar to the canonical van der Pol

oscillator [36,37]. There exists a trivial solution that loses stability at some critical parameter value, beyond which the system is attracted to a self-excited oscillation with nonzero amplitude. However, the formulation and analysis differ significantly from that associated with the van der Pol system. Moreover, the amplitude of the steady-state oscillation for the van der Pol equation grows like $\sqrt{\gamma - \gamma_\star}$, while in the present system the relationship between the amplitude and bifurcation parameter is no longer simple, as illustrated in Fig. 8.

4 Experimental comparison

The oscillator circuit was constructed on a two-layer PCB, with the intention of observing behavior at the V_G and V_S nodes as shown in Fig. 9. Steady-state oscillations of the implemented circuit were measured (see Fig. 10) using a DC voltage source to supply the drain voltage, an oscilloscope (Pico Technology 6402C) to measure the oscillating nodal voltages, and a spectrum analyser (Agilent N9030A) to measure the frequency response. As mentioned before, operational amplifiers (Texas Instruments LMH6609) in unity gain buffer configurations were used to mitigate electrical loading of the circuit while probing the output nodes. Numerical simulations of the circuit, performed with Cadence Spectre using built-in component models and the transistor model parameters from the datasheet [34], show a close match with the measured output. The measured frequency spectrum of the oscillator is presented in Fig. 11. Both the time domain and frequency response observations at steady state align well with expected Colpitts oscillator behavior.

Experimentally, the oscillator startup behavior was measured by connecting the voltage supply node (V_{dd}) in series with a magnetic reed switch (Coto Technology CT10-1530-G1) and then to the input power supply voltage. In order to start up the oscillator, a magnet was brought close to the reed switch, which connected the power supply bias voltage to the HEMT's drain. The nodal output voltages were sampled via the Pico Technology oscilloscope with long sample memory (128 Msamples were collected). The startup behavior is shown in Fig. 12 (only the envelope of the oscillations is visible due to the timescale in the figure). One can see that the amplitude of V_G in the experiment is close to 2 V, and the transient response also functions on the same qualitative timescale as the analysis. Differences can be

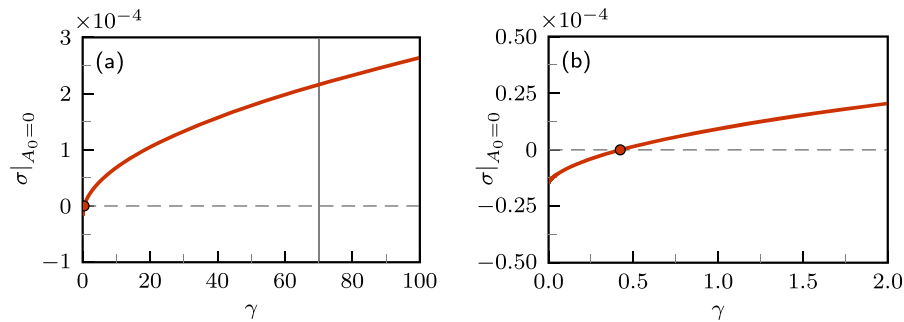


Fig. 7 Instantaneous growth rate $\sigma|_{A_0=0}$ of the trivial solution, as predicted from the multiple scales approach given in Eq. (30). If $\sigma|_{A_0=0} < 0$, then the trivial solution is stable, and for these parameters, the system is expected to be unsta-

ble for $\gamma > \gamma_* = 0.422$. For comparison, the thin vertical line at $\gamma = 70.00$ in Figure (a) corresponds to the parameter values simulated in Figs. 5–6. Figure (b) zooms in near the bifurcation point at $\gamma = \gamma_*$

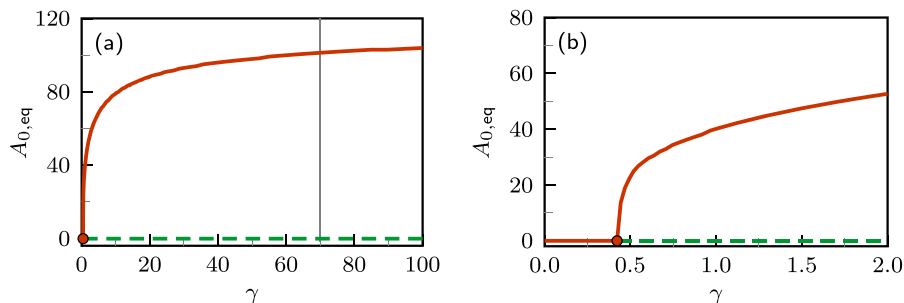


Fig. 8 Bifurcation diagram; steady-state amplitude vs. γ . Stable solutions are denoted with the solid line, while unstable branches are shown dashed. The bifurcation point is located

at $\gamma > \gamma_* = 0.422$. For comparison the thin vertical line at $\gamma = 70.00$ corresponds to the parameter values simulated in Figs. 5 and 6

accounted for due to the manufacturing variation—for example, the ATF-35143 HEMTs have significant part to part variation in gain and threshold voltage, and one can find combinations of those parameters that will better match the experimental results through the nondimensional parameter γ . However for the sake of using the multiple scales analysis as a design tool, we specifically show the response with the nominal parameter set given in Eq. (15).

5 Discussion and conclusions

The introduction of the harmonic balance solution within the multiple scales analysis leads to a complicated set of nonlinear algebraic equations, as illustrated in Appendix A. In the present system, the piecewise nature of the nonlinearity leads to a non-polynomial set of equations. Given the nonlinear function g_1 , one

can evaluate the integral terms by quadrature and again solve for the harmonic balance coefficients numerically. While this creates a reliance on numerical quadrature and the resulting numerical solution for the nonlinear algebraic system given in Eq. (33), this approach nonetheless leads to significant computational savings when compared with direct numerical simulation of the original equations of motion. It also allows for a wide variety of potential transistor models to be used.

The results arising from the multiple scales analysis presented here exhibit excellent agreement with direct numerical simulation of the derived equations of motion incorporating the piecewise continuous drain current model given in Eq. (6). Further, these predictions show good agreement with both the SPICE-based simulation and the experiment, validating the use of Eq. (6) to describe the nonlinearities of the FET. The GaAs HEMT device and quartz crystal resonator based

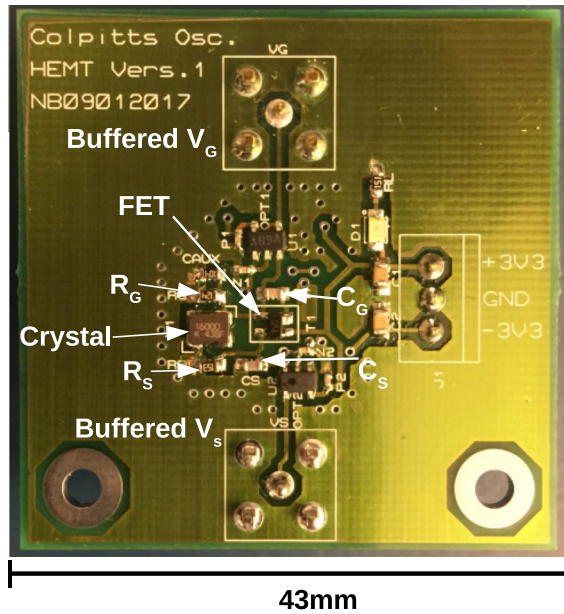


Fig. 9 Photograph of the circuit-board implementation of the Colpitts oscillator with important elements highlighted

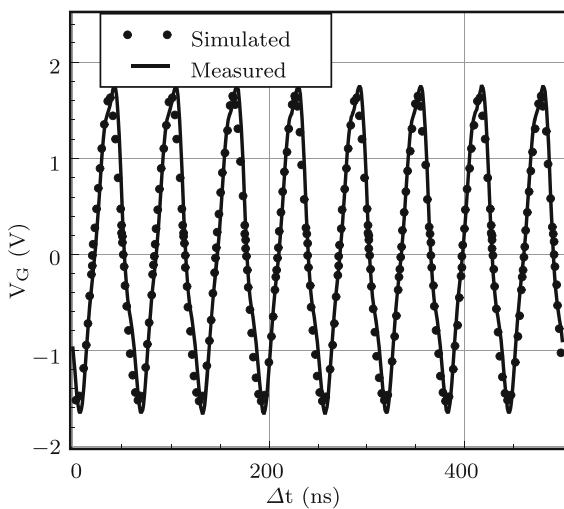


Fig. 10 Measured and simulated time-traces of the signal at the V_G node in steady state. Electrical loading due to the buffers was approximated with equivalent parasitic impedances in the simulated circuit (including an input resistance of 1.2 M Ω and input capacitance of 1.2 pF.) The measured response is not perfectly sinusoidal - there are certainly some unmodelled dynamics and some amplifier distortion may be present. However, agreement in amplitude appears good between the measured behavior and the Cadence Spectre simulation

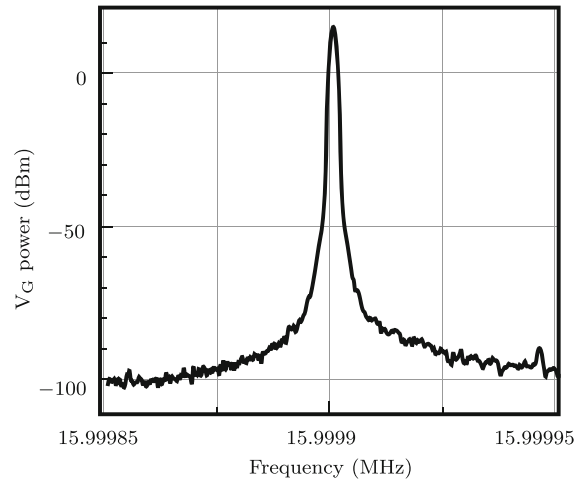


Fig. 11 Experimentally measured frequency spectrum of the oscillator, showing the fundamental oscillation frequency, measured with a signal analyser with a 50 Ω input impedance and 1 Hz resolution bandwidth

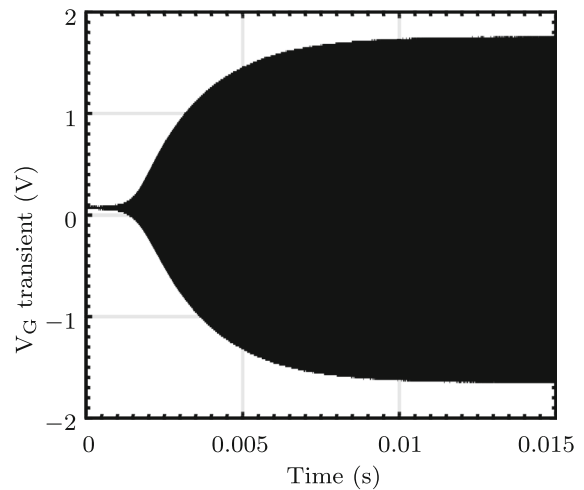


Fig. 12 Experimentally measured transient behavior of V_G , as the oscillator is switched on

Colpitts topology was shown to be practical to implement on a PCB. In particular, the analysis is able to capture the transient response of the Colpitts oscillator and can be used to explore the dependence of the observed behavior on the device parameters. As

expected, as the nondimensional gain is increased the oscillator exhibits self-excited oscillations and the analysis is able to describe the amplitude and frequency dynamics of the system. Moreover, the methodology developed for the present analysis is applicable to more general forms of the oscillator model, including more complicated forms of the nonlinear coupling through the FET. Future work will focus on scaling this modeling approach to N oscillators with various coupling mechanisms between the individual components and provide experimental verification of the behavior, in an effort to move towards fully integrated neurocomputing MEMS oscillator arrays.

Author contributions All authors contributed to the study conception and design. Material preparation, data collection and analysis were performed by S. Y. Shah, N. Bajaj, C. Pyles, and D. D. Quinn. The first draft of the manuscript was written by S. Y. Shah, N. Bajaj, and D. D. Quinn, and all authors commented on previous versions of the manuscript. All authors read and approved the final manuscript.

Funding: This material is based upon work supported by the National Science Foundation under Grants Nos. 1537988 and 1537701, the National Science Foundation Graduate Research Fellowship Program under Grant Number DGE-1333468, and the DARPA UPSIDE program under Grant No. 106661.

Data availability The datasets generated during and analysed during the current study are not publicly available but are available from the corresponding author on reasonable request. The datasets generated during and analysed during the current study are not publicly available but are available from the corresponding author on reasonable request.

Declarations

Competing interests: The authors have no relevant financial or non-financial interests to disclose.

Appendix A: Harmonic balance

The $\mathcal{O}(\varepsilon)$ equations for (u_1, v_1) on the η_0 timescale are solved using a harmonic balance approximation. Therefore, with the harmonic approximation given in Eq. (29) for (u_1, v_1) , the harmonic components of the piecewise defined nonlinearity identified as g_1 in Eq. (28) must be identified. Substituting Eq. (29) into Eq. (27), and equating coefficients of the harmonic terms yields

$$1: \quad \alpha_1 V = 0, \quad (33a)$$

$$\alpha_2 U = \frac{1}{2\pi} \int_0^{2\pi} g_1 d\psi_0, \quad (33b)$$

$\cos \psi_{1,0}$:

$$H - Y + \alpha_1 G = 0, \quad (33c)$$

$$-\mu H + (\mu + 1)Y + \alpha_2 X = \frac{1}{\pi} \int_0^{2\pi} g_1 \cdot \cos \psi_0 d\psi_0, \quad (33d)$$

$\sin \psi_{1,0}$:

$$-G + X + \alpha_1 H = -A_0, \quad (33e)$$

$$\mu G - (\mu + 1)X + \alpha_2 Y = \frac{1}{\pi} \int_0^{2\pi} g_1 \cdot \sin \psi_0 d\psi_0. \quad (33f)$$

Note that for $\varepsilon \gamma = 0$, the nonlinearity described by g_1 vanishes so that these equations are linear and can be solved. In this limit, the exponential growth rate [c.f., Eq. (32)] of the trivial solution ($A_0 \equiv 0$) can be evaluated in closed form, as given in Eq. (36). For $\varepsilon \gamma \neq 0$, this system of 6 coupled nonlinear algebraic equations must be solved numerically for (G, H, X, Y, U, V) as a function of A_0 , although note that $V = 0$.

Because of the inequality in the definition of the drain current, the integral terms in Eq. (33) are defined piecewise, depending on the value of $v_1 - u_1$, which for the harmonic approximation given in Eq. (29) is written as

$$v_1 - u_1 = (V - U) + (G - X) \cos \psi_0 + (H - Y) \sin \psi_0. \quad (34)$$

Nonetheless these integral terms can be numerically evaluated in terms of (G, H, U, V, X, Y) , so that Eq. (33) can then be solved for these harmonic balance coefficients as a function of the amplitude A_0 .

If the amplitude of $v_1 - u_1$ is not sufficient to reach the inequality, the harmonic balance equations for the nonlinear drain current reduce to Eq. (35). Regardless of the form of g_1 , the resulting solutions for (G, H) are returned to the evolution equations given in Eqs. (30–31) to approximate the amplitude and phase dynamics of the oscillator.

1:

$$0 = -\alpha_1 V, \quad (35a)$$

$$0 = -\alpha_2 U + 2\gamma (1 - u_0) (V - U)$$

$$+ \varepsilon \gamma \left[(V - U)^2 + \frac{(G - X)^2}{2} + \frac{(H - Y)^2}{2} \right], \quad (35b)$$

$\cos \psi_{1,0}$:

$$H - Y + \alpha_1 G = 0, \quad (35c)$$

$$- \mu H + (\mu + 1) Y + \alpha_2 X = 2\gamma$$

$$((1 - u_0) + \varepsilon (V - U)) (G - X), \quad (35d)$$

$\sin \psi_{1,0}$:

$$- G + X + \alpha_1 H = -A_0, \quad (35e)$$

$$\mu G - (\mu + 1) X + \alpha_2 Y = 2\gamma$$

$$\left((1 - u_0) + \varepsilon (V - U) \right) (H - Y). \quad (35f)$$

$$\sigma|_{A_0=0} \equiv \frac{1}{2}$$

$$\left(\frac{(1 - \alpha_1 (\alpha_2 + \Gamma)) (\alpha_2 + \Gamma) - (\alpha_1 (1 + \mu) + \alpha_2) (1 + \mu)}{(1 - \alpha_1 (\alpha_2 + \Gamma))^2 + (\alpha_1 (1 + \mu) + \alpha_2)^2} - \lambda \right),$$

with $\Gamma \equiv 2\gamma (1 - u_0)$. (36)

References

- Chang, H.-C., Cao, X., Mishra, U.K., York, R.A.: Phase noise in coupled oscillators: theory and experiment. *IEEE Trans. Microw. Theory Tech.* **45**(5), 604–615 (1997)
- Galton, I., Towne, D.A., Rosenberg, J.J., Jensen, H.T.: Clock distribution using coupled oscillators. In: *IEEE International Symposium on Circuits and Systems. Circuits and Systems Connecting the World: ISCAS 3*, 217–220 (1996)
- Vornicu, I., Carmona-Galán, R., Rodríguez-Vázquez, A.: Arrayable voltage-controlled ring-oscillator for direct time-of-flight image sensors. *IEEE Trans. Circuits Syst. I Regul. Pap.* **64**(11), 2821–2834 (2017)
- Nikonov, D.E., Csaba, G., Porod, W., Shibata, T., Voils, D., Hammerstrom, D., Young, I.A., Bourianoff, G.I.: Coupled-oscillator associative memory array operation for pattern recognition. *IEEE J. Explor. Solid-State Comput. Devices Circuits* **1**, 85–93 (2015)
- Hoppensteadt, F.C., Izhikevich, E.M.: Synchronization of laser oscillators, associative memory, and optical neurocomputing. *Phys. Rev. E* **62**(3), 4010–4013 (2000)
- Hoppensteadt, F., Izhikevich, E.: Synchronization of MEMS resonators and mechanical neurocomputing. *IEEE Trans. Circuits Syst. I: Fundam. Theory Appl.* **48**(2), 133–138 (2001)
- Yogendra, K., Fan, D., Roy, K.: Coupled spin torque nano oscillators for low power neural computation. *IEEE Trans. Magn.* **51**(10), 1–9 (2015)
- Cotter, M.J., Fang, Y., Levitan, S.P., Chiarulli, D.M., Narayanan, V.: Computational architectures based on coupled oscillators. In: *2014 IEEE Computer Society Annual Symposium on VLSI*, pp. 130–135 (2014)
- Strogatz, S.H.: From Kuramoto to Crawford: exploring the onset of synchronization in populations of coupled oscillators. *Physica D* **143**(1), 1–20 (2000)
- Dörfler, F., Bullo, F.: Synchronization in complex networks of phase oscillators: a survey. *Automatica* **50**(6), 1539–1564 (2014)
- Pikovsky, A., Rosenblum, M.: Dynamics of globally coupled oscillators: progress and perspectives. *Chaos: Interdiscip. J. Nonlinear Sci.* **25**(9), 097616 (2015)
- Fell, J., Axmacher, N.: The role of phase synchronization in memory processes, vol. 12, no. 2, p. 105 (2011)
- Maggio, G.M., Feo, O.D., Kennedy, M.P.: Nonlinear analysis of the Colpitts oscillator and applications to design. *IEEE Trans. Circuits Syst. I: Fundam. Theory Appl.* **46**(9), 1118–1130 (1999)
- Martens, E.A., Thutupalli, S., Fourrière, A., Hallatschek, O.: Chimera states in mechanical oscillator networks. *Proc. Natl. Acad. Sci.* **110**(26), 10563–10567 (2013)
- Matthews, P.C., Mirollo, R.E., Strogatz, S.H.: Dynamics of a large system of coupled nonlinear oscillators. *Physica D* **52**(2), 293–331 (1991)
- Shirasaka, S., Kurebayashi, W., Nakao, H.: Phase-amplitude reduction of transient dynamics far from attractors for limit-cycling systems. *Chaos: Interdiscip. J. Nonlinear Sci.* **27**(2), 023119 (2017)
- Poel, W., Zakharova, A., Schöll, E.: Partial synchronization and partial amplitude death in mesoscale network motifs. *Phys. Rev. E* **91**(2), 022915 (2015)
- Thornburg, K.S., Möller, M., Roy, R., Carr, T.W., Li, R.-D., Erneux, T.: Chaos and coherence in coupled lasers. *Phys. Rev. E* **55**(4), 3865–3869 (1997)
- Bahr, B.W., Popa, L.C., Weinstein, D.: 1 GHz GaN-MMIC monolithically integrated MEMS-based oscillators. In: *2015 IEEE International Solid-State Circuits Conference—(ISSCC) Digest of Technical Papers*, pp. 1–3 (2015)
- Li, M.-H., Chen, C.-Y., Li, C.-S., Chin, C.-H., Li, S.-S.: A monolithic CMOS-MEMS oscillator based on an ultra-low-power ovenized micromechanical resonator. *J. Microelectromech. Syst.* **24**(2), 360–372 (2015)
- Verd, J., Uranga, A., Abadal, G., Teva, J.L., Torres, F., López, J., Pérez-Murano, F., Esteve, J., Barniol, N.: Monolithic CMOS MEMS oscillator circuit for sensing in the attogram range. *IEEE Electron Device Lett.* **29**(2), 146–148 (2008)
- Agrawal, D.K., Woodhouse, J., Seshia, A.A.: Observation of locked phase dynamics and enhanced frequency stability in synchronized micromechanical oscillators. *Phys. Rev. Lett.* **111**(8), 084101 (2013)
- Matheny, M.H., Grau, M., Villanueva, L.G., Karabalin, R.B., Cross, M., Roukes, M.L.: Phase synchronization of two anharmonic nanomechanical oscillators. *Phys. Rev. Lett.* **112**(1), 014101 (2014)
- Kennedy, M.P.: Chaos in the Colpitts oscillator. *IEEE Trans. Circuits Syst. I: Fundam. Theory Appl.* **41**(11), 771–774 (1994)
- Volos, C.K., Pham, V.T., Vaidyanathan, S., Kyprianidis, I.M., Stouboulos, I.N.: Synchronization phenomena in cou-

- pled Colpitts circuits. *J. Eng. Sci. Technol. Rev.* **8**(2), 142–151 (2015)
26. De Feo, O., Maggio, G.M.: Bifurcations in the Colpitts oscillator: from theory to practice. *Int. J. Bifurc. Chaos* **13**(10), 2917–2934 (2003)
 27. Agrawal, D.K., Woodhouse, J., Seshia, A.A.: Modeling nonlinearities in MEMS oscillators. *IEEE Trans. Ultrasonics Ferroelectrics Freq. Control* **60**(8), 1646–1659 (2013)
 28. Agrawal, D.K., Woodhouse, J., Seshia, A.A.: Synchronization in a coupled architecture of microelectromechanical oscillators. *J. Appl. Phys.* **115**(16), 164904 (2014)
 29. Vittoz, E.A., Degrauwe, M.G.R., Bitz, S.: High-performance crystal oscillator circuits: theory and application. *IEEE J. Solid-State Circuits* **23**(3), 774–783 (1988)
 30. Liu, Y., Cai, Y., Zhang, Y., Tovstopyat, A., Liu, S., Sun, C.: Materials, design, and characteristics of bulk acoustic wave resonator: a review. *Micromachines* **11**(7), 630 (2020)
 31. Larson, J.D., Bradley, P.D., Wartenberg, S., Ruby, R.C.: Modified Butterworth-Van Dyke circuit for FBAR resonators and automated measurement system. In: 2000 IEEE Ultrasonics Symposium. Proceedings. An International Symposium (Cat. No.00CH37121), San Juan, PR, USA, vol. 1, pp. 863–868 (2000)
 32. Li, M., Seok, S., Rolland, N., Rolland, P.A., El Aabbaoui, H., De Foucauld, E., Vincent, P., Giordano, V.: Ultralow-phase-noise oscillators based on BAW resonators. *IEEE Trans. Ultrasonics Ferroelectrics Freq. Control* **61**:6 (2014)
 33. Statz, H., Newman, P., Smith, I.W., Pucel, R.A., Haus, H.A.: GaAs FET device and circuit simulation in SPICE. *IEEE Trans. Electron Devices* **34**(2), 160–169 (1987)
 34. Broadcom: Low noise pseudomorphic HEMT in a surface mount plastic package. ATF-35143 datasheet (2012)
 35. Chatterjee, A.: Harmonic balance based averaging: approximate realizations of an asymptotic technique. *Nonlinear Dyn.* **32**(4), 323–343 (2003)
 36. Nayfeh, A.H., Mook, D.T.: *Nonlinear Oscillations*. Wiley-VCH Verlag GmbH, Weinheim (2007)
 37. Rand, R.H.: *Topics in Nonlinear Dynamics with Computer Algebra*. Gordon and Breach Science Publishers Inc, Newark (1994)

Publisher's Note Springer Nature remains neutral with regard to jurisdictional claims in published maps and institutional affiliations.

Springer Nature or its licensor (e.g. a society or other partner) holds exclusive rights to this article under a publishing agreement with the author(s) or other rightsholder(s); author self-archiving of the accepted manuscript version of this article is solely governed by the terms of such publishing agreement and applicable law.